Supplementary Information

A. Optical spectra

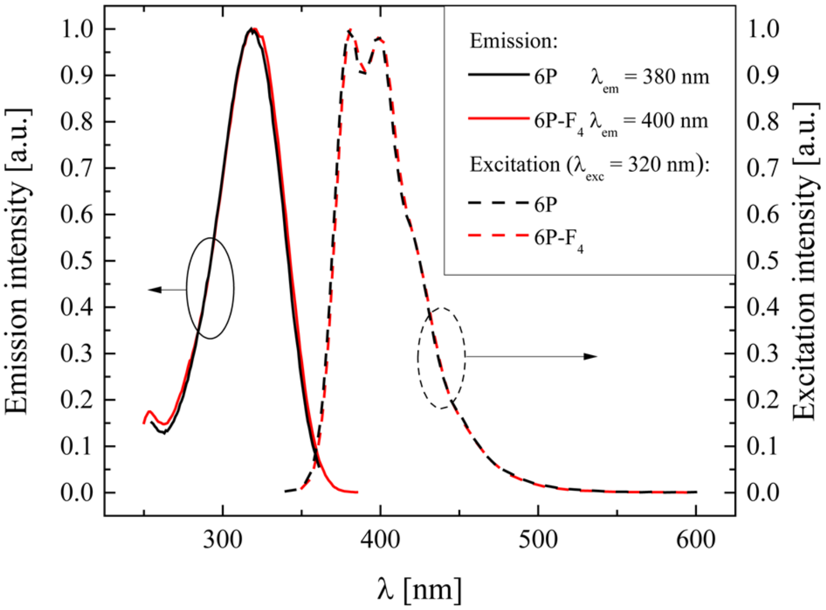

Fig. S1: Excitation (solid line) and corresponding fluorescence (dashed line) spectra of 6P and 6P-F_4 in $CHCl_3$ at 25 °C with the spectra normalized to 1.

Figure S1 compares fluorescence emission and excitation spectra of 6P and 6P-F4. Due to the poor solubility, the optical density is insufficient to measure absorption spectra (for more detail see Garmshausen et al.[1]). Both, fluorescence emission and excitation spectra almost perfectly coincide proving that fluorination does not affect the optical properties of para-sexiphenyl.

B. Synthesis of 6P-F$_4$

Ethyl acetate, methylene chloride, petroleum ether, ethanol, and toluene were distilled before usage. All other starting materials were used as received. NMR spectra were recorded on a Bruker DPX 300 Spectrometer (300 MHz for ^{1}H, 75 MHz for ^{13}C, and 282 MHz for ^{19}F) at 25 °C using residual protonated solvent signals as internal standard (^{1}H: δ($CHCl_3$) = 7.26 ppm; ^{13}C: δ($CDCl_3$) = 77.16 ppm; and $CFCl_3$ as external standard for ^{19}F-NMR spectra. For column chromatography silica gel (0.035-0.070 mm, 60 Å pore size) was used.

Synthesis of 3,3’’’’’,5,5’’’’’-tetrafluoro-*p*-sexiphenyl (6P-F$_4$) was accomplished via Ni-catalyzed homocoupling of the intermediate 3’’,5’’-difluoro-4-bromo-*p*-terphenyl as summarized in Figure S2.

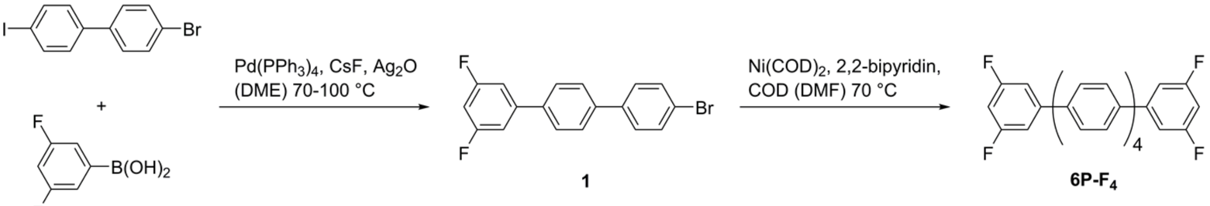

Figure S2: Synthetic route to 3,3’’’’’,5,5’’’’’-tetrafluoro-*p*-sexiphenyl (6P-F$_4$).

Synthesis of 4-bromo-3’’,5’’-difluoro-*p*-terphenyl (1):

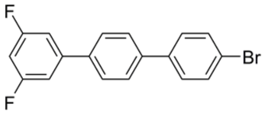

1

Under an argon atmosphere 4-bromo-4’-iodobiphenyl[2] (2.1 g, 5.9 mmol) was dissolved in 15 mL of 1,2-dimethoxyethane and argon was bubbled through the solution for 10 min. 3,5-Difluorophenylboronic acid (770 mg, 4.9 mmol), CsF (1.5 g, 9.8 mmol), Pd(PPh_3)$_4$ (170 mg, 0.15 mmol) and Ag_2O (1.4 g, 5.9 mmol) were added. The suspension was stirred at 70 °C for 5 h and overnight at 100 °C. After cooling to room temperature the mixture was added to Celite© and the crude product extracted from the Celite© using hot toluene. The organic phase was washed with brine and dried over anhydrous $MgSO_4$. Evaporation of the solvent under reduced pressure and column chromatography using petroleum ether yielded the product as white crystals (918 mg, 2.7 mmol, 55%). ^{1}H-NMR (300 MHz, $CDCl_3$): δ [ppm]= 6.81 (tt, ^3J(C-F)= 8.9 Hz, ^4J= 2.3 Hz ,1H), 7.14 (m, 2H), 7.50 (m, 2H), 7.59 (m, 2H) 7.64 (m, 4H). ^{13}C-NMR (75 MHz, $CDCl_3$): δ [ppm]= 109.8, 110.1, 122.1, 127.6, 128.8, 132.2. ^{19}F-NMR (282 MHz, $CDCl_3$): δ [ppm]= 109.81 (dd ^3J_a(C-F)= 8.9 Hz, ^3J_b(C-F)= 8.9 Hz, 2F). λ(abs)$_{max}$ ($CHCl_3$, 25 °C): 284.5 nm.

Synthesis of 3,3’’’’’,5,5’’’’’-tetrafluoro-*p*-sexiphenyl (6P-F_4):

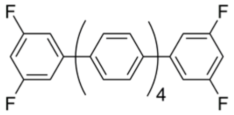

6P-F_4

In a glove box 4-bromo-3’’,5’’-difluoro-*p*-terphenyl **1** (900 mg, 2.6 mmol), 2,2-bipyridin (450 mg, 2.9 mmol), Ni(COD)$_2$ (660 mg, 2.4 mmol), and COD (0.9 mL, 7.5 mmol) were suspended in 22 mL of DMF. The mixture was stirred at 70 °C for 44 h. After cooling to room temperature the mixture was filtered and washed with ethanol, water, and a mixture of concentrated HCl (50 mL) in ethanol (280 mL). The grey precipitate was washed with further ethanol, petroleum ether, ethyl acetate, and methylene chloride. The residue was recrystallized from nitrobenzene and 1,2,4-trichlorobenzene to afford the product as colorless crystals (469 mg, 0.9 mmol, 34%). EA calculated for $C_{36}H_{22}F_4$: C: 81.50%, H: 4.18%, found: C: 81.79%, H: 4.10%. EI-MS *m/z* calculated for $C_{36}H_{22}F_4$ [M$^+$]: 530.1658, found: 530.1658. $\lambda(\text{exc})_{\text{max}}$ ($CHCl_3$, 25 °C, emission: 400 nm): 320 nm, $\lambda(\text{emi})_{\text{max}}$ ($CHCl_3$, 25 °C, excitation: 320 nm): 381.0 nm, 399.5 nm.

C. Height Profile of scratched region

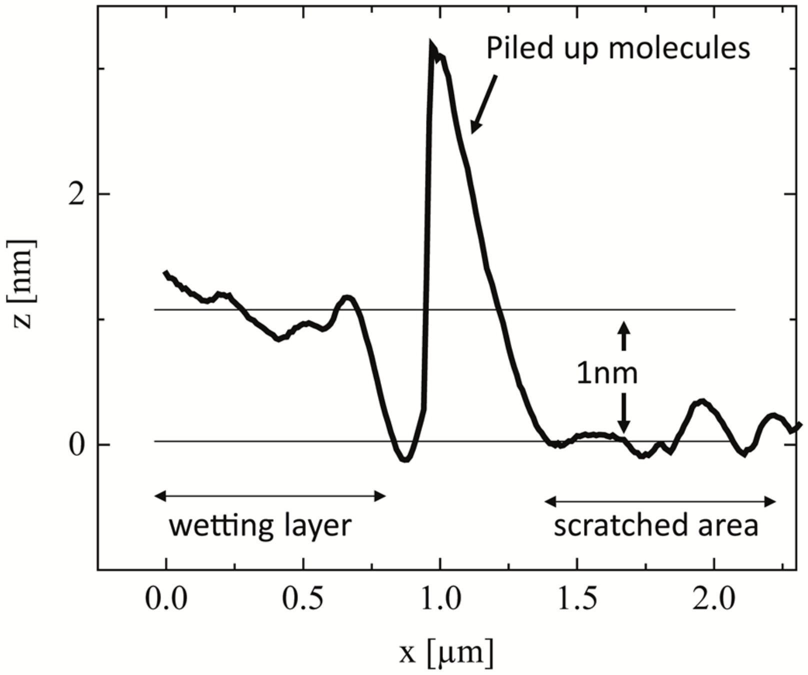

Fig. S3: Cross-section profile over the scratched area of the 6P-F_4 sample in Fig. 3 after an exposure time of 10 min.

A non-contact AFM scan over a scratched area of 2x2 µm² shows a trench of a about 1 nm in depth. The line scan (Fig. S3) indicates how the molecular layer is piled up at the edges of the trench. This suggests the formation of a wetting layer following the surface morphology of the ZnO substrate.

D. Surface induced structure 6P-F$_4$: *in situ* in-plane structure

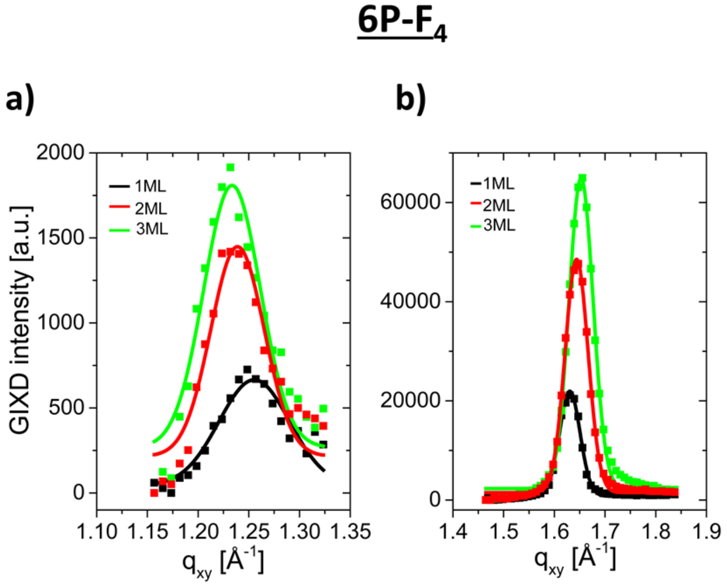

Fig. S4: *In situ* analysis of the in-plane structure of 6P-F$_4$. Both investigated peaks clearly shift with increasing film thickness.

The *in situ* analysis of the in-plane crystal structure of 1, 2 and 3ML thick 6P-F$_4$ films confirms that the surface induces a new structure in the first 6P-F$_4$ monolayers. The position of two 6P-F$_4$ in-plane Bragg reflections measured in grazing incidence diffraction (GIXD) geometry were investigated as a function of coverage (see Fig. S4). A shift in opposite directions was found for the two peaks with increasing film thickness. The position of the peak shown in Fig. S4a shifts to lower q_{xy} values from q_{xy}=1.26 Å^{-1} (1ML) to q_{xy}=1.21 Å^{-1} (3ML). In contrast the second peak (Fig. S4b) shifts towards larger q_{xy} values starting from q_{xy}=1.63 Å^{-1} (1ML) and reaching q_{xy}=1.67 Å^{-1} (3ML). Although we cannot index the two reflections because of the unknown 6P-F$_4$ unit cell, their shift clearly implies a surface induced structure, supporting the information gained from the shift of the out-of-plane reflection.

		1 ML	**2 ML**	**3 ML**
Peak a)	q_{xy} [Å^{-1}]	1.26	1.23	1.21
	d [nm]	0.499	0.511	0.519
Peak b)	q_{xy} [Å^{-1}]	1.63	1.65	1.67
	d [nm]	0.385	0.381	0.376

Table S1: Values of the shifting in-plane Bragg peaks of 6P-F$_4$ measured *in situ*.

E. Trofimov model

Interferences between successively growing monolayers lead to temporal oscillations of the reflected intensity at fixed q_z points during thin-film growth. This can be seen directly from the equation for the reflected intensity $I_{reflected}(t)$, as calculated in kinematic approximation:

$$I_{reflected}(t) = \left| A_{substrate}(q_z) \times e^{i\varphi(q_z)} + f(q_z) \times \sum_n \theta_n(t) e^{inq_z d} \right|^2. \tag{1}$$

$A_{substrate}(q_z)$: substrate scattering amplitude

$f(q_z)$: molecular form factor

$\varphi(q_z)$: phase between substrate and ad-layer scattering

n: layer number

θ_n: fractional coverage of the n'th-layer

q_z: X-ray wave-vector transfer upon reflection

d: out-of-plane lattice spacing within the crystalline thin film.

For a quantitative analysis of the growth and theoretical modelling of the X-ray data both the above calculation of the X-ray scattering as well as a growth model for the temporal evolution of θ_n is needed. In the past different growth models have been successfully applied to describe the growth of a number of different molecular thin-films.[3–6] The growth model we use in this paper is based on a distributed growth model proposed by Trofimov *et al.*.[7] However, the original model by Trofimov describes the growth in both the in- and out-of-plane directions. Therefore a simplification is needed prior to applying this model to our experimental data, where only the film growth in the out-of-plane direction is investigated.

The simplified Trofimov model describes the growth process only via the growth rate R_n and the effective critical layer coverage $\theta_{n,cr}$ of each layer as shown in eq. (2)-(3). The critical layer coverage of the n'th layer $\theta_{n,cr}$ gives the coverage θ_n of the layer before the n+1'th layer starts to nucleate and to grow on top of the n'th layer. The feeding zone parameter ξ_n marks the size (in units of coverage) of the zone on top of the n'th layer where molecules will contribute to nucleation and growth of the n+1'th layer as opposed to the region outside the feeding zone where molecules will diffuse over the edge into the n'th layer. The rate equation then reads:

$$\frac{d\theta_n}{dt} = \begin{cases} R_1(1-\theta_1) + R_{n>1}(\theta_1 - \xi_1), n = 1 \\ R_{n>1}(\xi_{n-1} - \xi_n), n > 1, \end{cases} \tag{2}$$

with the size of the feeding zone given by

$$\xi_n = \begin{cases} 0, \theta_n < \theta_{cr,n} \\ 1 - e^{-\left[\sqrt{-\ln\left(1-\theta_n\right)} - \sqrt{-\ln\left(1-\theta_{cr,n}\right)}\right]^2} \end{cases} \qquad (3)$$

Using the Trofimov model we fit the growth oscillations for both 6P and 6P-F_4 simultaneously at three different q_z points as discussed in the main text. This allows us to further constrain the fit parameters since only $A_{substrate}$, φ and f differ for the fits at different q_z points. We also gain additional information from the oscillations at higher q_z values. For example during the 6P growth the Anti-Bragg oscillations are strongly damped due to the fast roughening of the film. But together with the oscillations at larger q_z values a fit of the physical parameters such as ML thickness and ML growth rate within the Trofimov model is still possible even when the Anti-Bragg oscillations are damped out.

In Fig. 6 in the main text the red lines represent the best fits based on the Trofimov model to the experimental values shown as dots. The complete set of the obtained fit parameters can be found in table S2 for both 6P and 6P-F_4.

Trofimov fit parameters			
6P		**6P-F$_4$**	
$A_{substrate}$	1.00	$A_{substrate}$	1.00
φ	3.67	φ	2.58
f	0.38	f	0.49
d	2.693	$d_{1.ML}$	2.646
R_1	8.45E-04	$d_{2.ML}$	2.592
R_2	8.45E-04	$d_{3.ML}$	2.531
R_3	8.45E-04	$d_{4.ML}$	2.479
$R_{n>3}$	8.45E-04	$d_{5.ML}$	2.463
$\theta_{cr,1}$	0.324	$d_{6.ML}$	2.463
$\theta_{cr,2}$	0.060	$d_{7.ML}$	2.463
$\theta_{cr,3}$	0.023	$d_{8.ML}$	2.214
$\theta_{cr,4}$	0.017	R_1	3.73E-04
$\theta_{cr,5}$	0.008	R_2	3.92E-04
$\theta_{cr,6}$	0.008	R_3	4.32E-04
$\theta_{cr,7}$	0.002	$R_{n>3}$	4.44E-04
$\theta_{cr,8}$	0.002	$\theta_{cr,1}$	0.36
		$\theta_{cr,2}$	0.30
		$\theta_{cr,3}$	0.24
		$\theta_{cr,4}$	0.19
		$\theta_{cr,5}$	0.17
		$\theta_{cr,6}$	0.13
		$\theta_{cr,7}$	0.09
		$\theta_{cr,8}$	0.05

Table S2: Trofimov fit parameters used for the fits shown in Fig. 7 in the main text.

For 6P-F$_4$ the best fits were achieved for a decreasing lattice spacing *d* of each consecutive ML. The lattice spacing of the 1st ML is fitted to be 2.65 nm and decreases to 2.21 nm in the 8th ML, which implies an increasing molecular tilt angle (that is less upright standing molecules in higher layers). Thus, the trend of an increasing molecular tilt angle for higher ML is confirmed by the Trofimov model approach. Comparing the absolute values of the lattice spacing with the one obtained from the higher order Bragg reflections (s. table 1 in the main text) we find a small difference of about 5 % for the *d* values of the 2nd and 3rd ML. Note that the determination of the layer spacing is more accurate by investigating the positions of the higher order Bragg peaks. In the Trofimov model the dependencies of the parameters on each other may be the reason for the small deviations of the *d* values from the one given in in Fig. 5 in the main text.

The fit parameters reveal that there is an increase in the growth rate of each single ML in the case of 6P-F_4. The first ML which grows directly on the bare ZnO substrate has the slowest growth rate of $3.7{\cdot}10^{-4}$ ML/molec. exposure. It increases then gradually to a constant value of $4.4{\cdot}10^{-4}$ ML/molec. exposure from the fourth ML on. One of the reasons for the slow first ML growth rate could be related with the formation of the wetting layer in the early stages of the growth as shown in the analysis by AFM in the main text. For 6P no evidence for a surface induced structure was found and the best fits were realized with a constant ML thickness of 2.69 nm and a constant ML growth rate of $8.5{\cdot}10^{-4}$ (ML/molec. exposure) (see Table S2).

F. Parratt-Fits

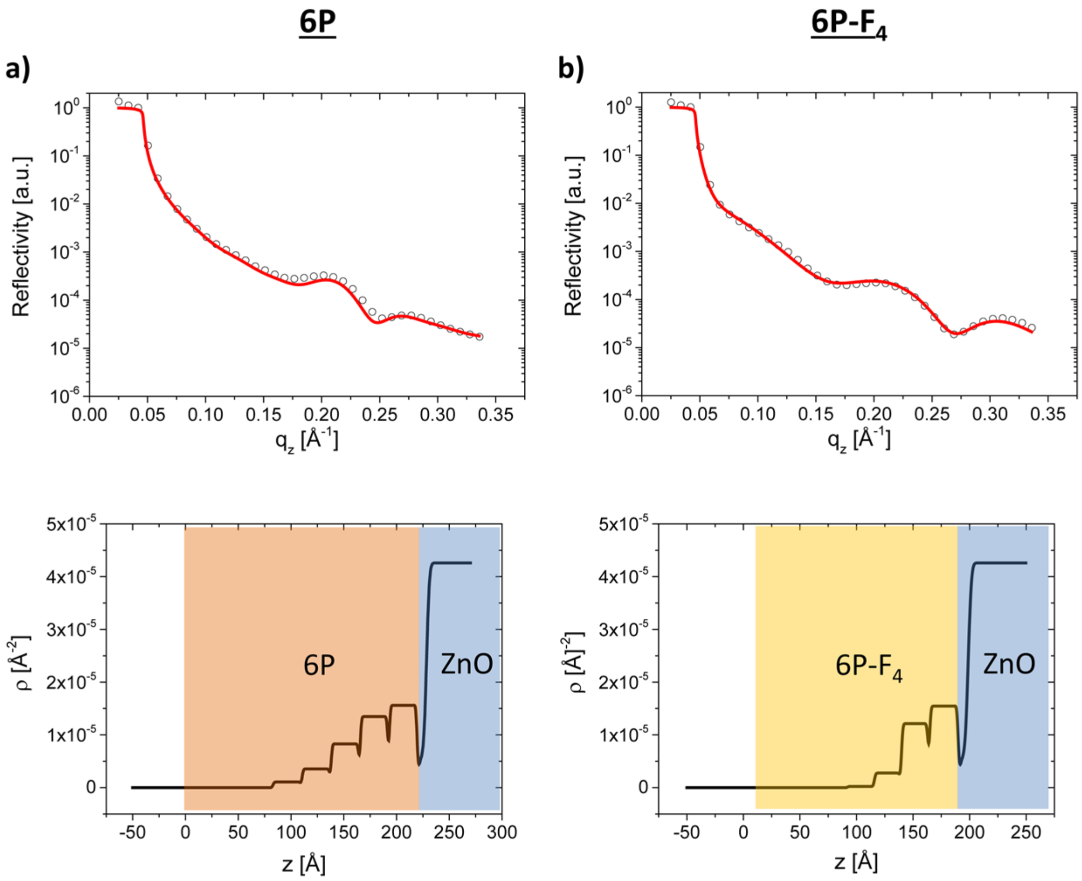

Fig. S5: Comparison of two 6P and 6P-F_4 films with similar coverages of the first and second monolayer. Top: XRR curves of 6P (a) and 6P-F_4 (b) films (dots) with the corresponding Parratt fits (red lines). Bottom: scattering length density curves of 6P (a) and 6P-F_4 (b). 6P films need to be grown much thicker than 6P-F_4 until the scattering length density (that is coverage) in the first two monolayers is the same. Put differently 6P grows much rougher and multiple layers grow before the second monolayer is filled.

In the top part of Fig. S5 exemplary XRR curves acquired *in situ* during the growth of 6P (a) and 6P-F_4 (b) are shown. By fitting each *in situ* XRR curve based on the Parratt formalism[8] (red curves in Fig. S5), one can quantify for every single molecular ML the scattering length density ρ (i.e. electron density times the Thomson scattering length) and the ML thickness using a 'box' scattering length density model as shown in the bottom of Fig S5. The scattering length density of the ML *n* is a measure for the coverage of ML *n*. Hence the temporal evolution of each of these parameters and, thus, of the out-of-plane film morphology can be investigated. The exact fit parameters for the two exemplary curves are listed in table S3. As can be seen from these fit parameters we had to include in both cases an initial layer on the ZnO substrate. This initial layer accounts for residual adsorbents like H_2O, OH-groups etc. which are present on the reactive ZnO surface prior to the thin-film deposition. The thickness, roughness and scattering length density of this initial molecular coverage was obtained from Parratt fits of respective XRR curves acquired before film deposition. These parameters were then kept constant for the fits of the XRR curves acquired during thin-film growth. For the scattering length density of ZnO itself tabulated values from the NIST database were inserted into the fit model. To simulate the scattering length density modulation due to the molecular layers, we included into the fit models for the *in situ* XRR curves of both molecules a spacer layer between each ML with a total thickness of 0.1 nm (0.05 nm on top and 0.05 nm from the bottom ML) and a fixed scattering length density of $\rho=0.0$ Å^{-2}. Thus, to obtain the real lattice spacing of each ML one has to add 0.1 nm to the thickness of each ML shown in table S1. The first ML of 6P-F_4 has hence a *d* value of 2.64 nm, the second ML a *d* value of 2.48 nm and the third one a *d* of 2.40 nm. This is in very good agreement with the values obtained from the positions of the higher order Bragg peaks shown in table 1 in the main text and it also confirms the increasing tilt angle of the molecules at higher MLs.

6P

a)

	d [Å]	ρ [Å^{-2}]	σ [Å]
spacer layer	0.5	0.00E+00	1
8ML	26.5	0.00E+00	1
spacer layer	1	0.00E+00	1
7ML	26.5	0.00E+00	1
spacer layer	1	0.00E+00	1
6ML	26.5	0.00E+00	1
spacer layer	1	0.00E+00	1
5ML	26.5	1.07E-06	1
spacer layer	1	0.00E+00	1
4ML	26.5	3.54E-06	1
spacer layer	1	0.00E+00	1
3ML	26.5	8.30E-06	1
spacer layer	1	0.00E+00	1
2ML	26.5	1.35E-05	1
spacer layer	1	0.00E+00	1
1ML	26.5	1.56E-05	1
spacer layer	1	0.00E+00	1
intial adsorbants	7.94	5.59E-06	1.631
ZnO	-	4.26E-05	2.172

6P-F$_4$

b)

	d [Å]	ρ [Å^{-2}]	σ [Å]
spacer layer	0.5	0.00E+00	1
8ML	20	0.00E+00	1
spacer layer	1	0.00E+00	1
7ML	21.96	0.00E+00	1
spacer layer	1	0.00E+00	1
6ML	22.51	0.00E+00	1
spacer layer	1	0.00E+00	1
5ML	23.19	0.00E+00	1
spacer layer	1	0.00E+00	1
4ML	22.64	2.29E-07	1
spacer layer	1	0.00E+00	1
3ML	22.97	2.77E-06	1
spacer layer	1	0.00E+00	1
2ML	23.77	1.21E-05	1
spacer layer	1	0.00E+00	1
1ML	25.37	1.55E-05	1
spacer layer	1	0.00E+00	1
intial adsorbants	7.94	5.59E-06	1.631
ZnO	-	4.26E-05	2.172

Table S3: Parameters used to obtain Parratt fits of the XRR curves acquired *in situ* and in real-time during thin-film growth for 6P (a) and 6P-F$_4$ (b).

In Fig. S6 a 3D plot of the XRR curves calculated by the Parratt model for 6P and 6P-F$_4$ is shown, which illustrates the temporal evolution of the X-ray reflectivity in our model. The comparison of this simulated 3D plot with the temporal evolution of experimental XRR curves (Fig. 4 in the main text) underlines the overall good fit quality throughout the complete deposition time.

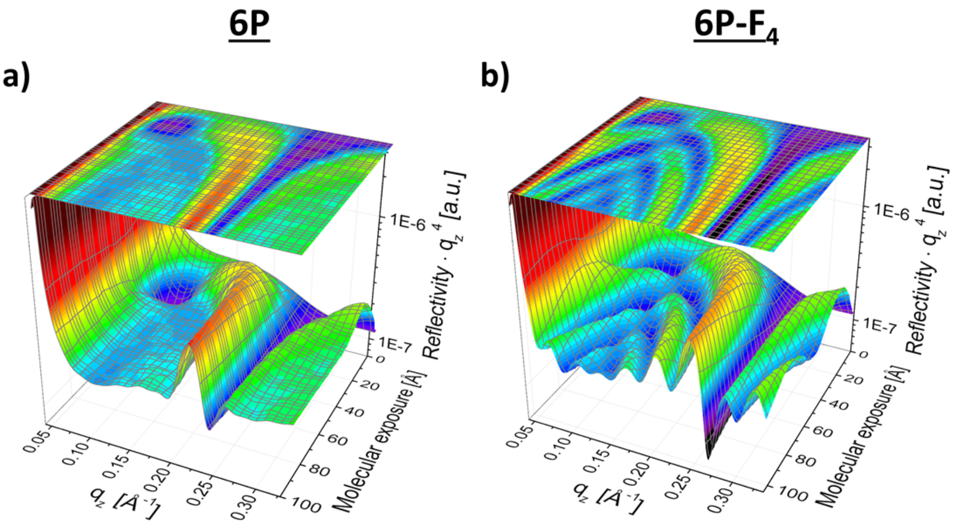

Fig. S6: Temporal evolution of the Parratt fitted XRR curves for the deposition of 6P (a) and 6P-F4 (b) on ZnO (10-10).

References

1. Y. Garmshausen, J. Schwarz, J. Hildebrandt, B. Kobin, M. Pätzel, and S. Hecht, *Org. Lett.*, 2014, **16**, 2838–41.

2. R. D. Hreha, Y.-D. Zhang, B. Domercq, N. Larribeau, J. N. Haddock, B. Kippelen, and S. R. Marder, *Synthesis (Stuttg).*, 2002, 1201–1212.

3. B. Krause, F. Schreiber, H. Dosch, A. Pimpinelli, and O. H. Seeck, *Europhys. Lett.*, 2004, **65**, 372–378.

4. A. R. Woll, T. V. Desai, and J. R. Engstrom, *Phys. Rev. B*, 2011, **84**, 075479.

5. A. Amassian, T. V Desai, S. Kowarik, S. Hong, A. R. Woll, G. G. Malliaras, F. Schreiber, and J. R. Engstrom, *J. Chem. Phys.*, 2009, **130**, 124701.

6. S. Y. An, K. Ahn, D. Y. Kim, H.-H. Lee, J. H. Cho, and D. R. Lee, *J. Chem. Phys.*, 2014, **140**, 154702.

7. V. I. Trofimov and V. G. Mokerov, *Thin Solid Films*, 2003, **428**, 66–71.

8. L. Parratt, *Phys. Rev.*, 1954, **95**, 359–369.